An Enhanced Distributed Control Architecture of Multiple Three-Phase PMSG for Improving Redundancy

Ge Liang, Sheng Huang, Wu Liao, Yu Liu, *Graduate Student Member, IEEE*, Congqi Feng, *Graduate Student Member, IEEE*, Xuan Wu, and Shoudao Huang, *Senior Member, IEEE*

***Abstract*—Multiple three-phase permanent magnet synchronous generator (MTP-PMSG) has excellent fault-tolerant features in theory. However, the commonly used control architectures, such as the centralized control architecture with only one central controller and the distributed control architecture where the interconnected communication cables between controllers may fail, limit the fault tolerance of MTP-PMSG. Therefore, this article proposes an enhanced distributed control (EDC) architecture without interconnected communication cables of MTP-PMSG for improving redundancy. The sensorless control and harmonic current suppression algorithm are considered and implemented in the EDC architecture. First, this article analyzes the magnetic field coupling between the winding sets of MTP-PMSG, and the variation law of equivalent inductance of the winding sets under the condition of arbitrary current sharing is obtained. Then, an enhanced distributed sensorless control method in EDC architecture is proposed based on the equivalent inductance. Furthermore, this article proposes a model-free predictive harmonic current suppression method to solve the MTP-PMSG's inherent harmonic problem in the EDC architecture. The effectiveness of the proposed methods is verified by the comparative simulations and experiments in a dual three-phase PMSG with arbitrary current sharing of winding sets.**

***Index Terms*—Distributed control, model-free predictive control, multiple three-phase permanent magnet synchronous generator (MTP-PMSG), sensorless control.**

I. Introduction

OFFSHORE wind power has the advantages of higher and steadier power quality, lower cost per kilowatt hour, and no occupation of land resources compared with onshore wind power, which is gradually the research focus of many research institutions [1], [2]. However, the offshore wind power generation system always operates in the harsh marine environment of high humidity and high salt fog. In addition, the offshore wind power system is far away from land, which makes operation and maintenance more difficult than the onshore wind power. Therefore, the offshore wind power generation system has extremely strict requirements on reliability and fault tolerance [3].

Compared with the conventional three-phase permanent magnet synchronous generator (PMSG), the multiple three-phase PMSG (MTP-PMSG) has multiple winding sets, which can be fed by multiple converters. It can continue to operate even if one/more windings or inverters are broken, which has inherently fault tolerance [4], [37]. This advantage makes the MTP-PMSG more suitable for remote high-power offshore wind power generation systems [5], [6]. Currently, there are many multiphase machines used in the wind power generation system, such as six-phase machines [7], nine-phase machines [8], twelve-phase machines [9], and so on.

The MTP-PMSG can generally be controlled following two methods: vector space decomposition (VSD) and multi-dq modeling. According to the VSD method, the fundamental, harmonic, and zero-sequence components of MTP-PMSG are projected to mutually orthogonal subspaces [10], [32]. Then, the MTP-PMSG can be controlled in these subspaces without coupling. However, the VSD method becomes complex with an increasing number of MTP-PMSG phases. The multi-dq modeling method is another well-known model for the MTP-PMSG. Based on the multi-dq modeling method, the MTP-PMSG is regarded as the combination of individual three-phase PMSG, and then the control strategy of conventional three-phase PMSG can be used to operate the MTP-PMSG. However, when the multi-dq modeling method is applied, the voltage equation will contain complex coupling terms due to the flux linkage coupling phenomenon of MTP-PMSG [11], which increases the difficulty of decoupling control.

Corresponding to the above-mentioned two control methods, there are two control architectures for multiple three-phase generators: centralized and distributed control architectures. Most control algorithms, such as vector control, direct torque control, sensorless control, and so on, can be implemented in these two control architectures. The schematic diagrams of the centralized and conventional distributed control architecture for

Manuscript received 20 February 2023; revised 24 May 2023; accepted 18 June 2023. Date of publication 20 June 2023; date of current version 28 July 2023. This work was supported in part by the National Natural Science Foundation of China under Grant 52107045, and in part by the National Key Research and Development Program of China under Grant 2022YFB4201503. Recommended for publication by Associate Editor S. Panda. *(Corresponding author: Wu Liao.)*

The authors are with the College of Electrical and Information Engineering, Hunan University, Changsha 410082, China (e-mail: lg1213@hnu.edu.cn; huangsheng319@hnu.edu.cn; liaowu1988@hnu.edu.cn; liuyu1996@hnu.edu.cn; fengcongqi99@hnu.edu.cn; wuxuan@hnu.edu.cn; hsd1962@hnu.edu.cn).

Color versions of one or more figures in this article are available at https://doi.org/10.1109/TPEL.2023.3288049.

Digital Object Identifier 10.1109/TPEL.2023.3288049

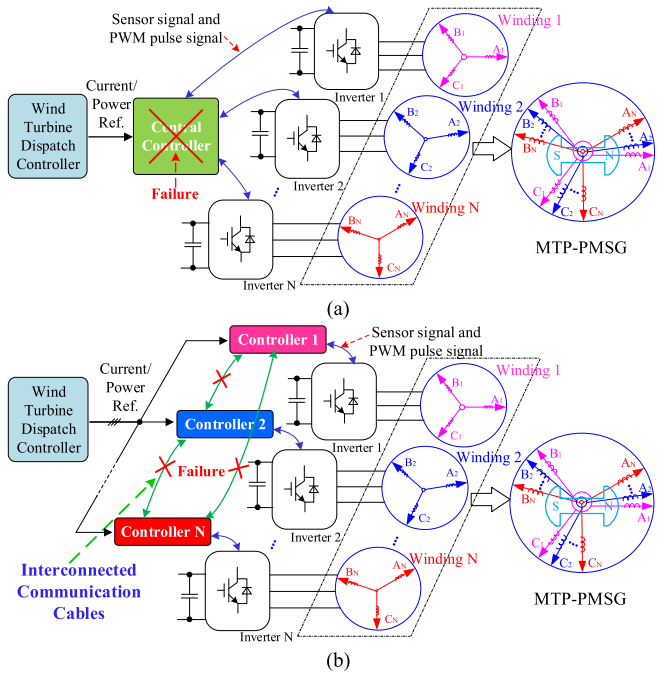

Fig. 1. Control architectures for MTP-PMSG in offshore wind power systems. (a) Centralized control architecture. (b) Conventional distributed control architecture with interconnected communication cables.

offshore wind power systems are presented in Fig. 1(a) and (b), respectively. The centralized control architecture operates with a single central controller that comprehensively receives and processes all measurement information, including current and rotor position data, and generates pulsewidth modulation (PWM) signals to control the MTP-PMSG [10], [13], [33], [34], [36]. This architecture offers improved centralization and comprehensive system information processing. However, it exhibits relatively lower redundancy and fault-tolerance performance [34]. In contrast, the conventional distributed control architecture employs individual controllers for each three-phase winding set. These controllers receive current information for their respective windings and exchange data, such as current and rotor position information, through interconnected communication cables to achieve effective decoupling [14], [25], [34], [35], [36]. This architecture exhibits strong redundancy and reliability, but its controllability is limited by the low degrees of control freedom, making it impossible to control the subspaces of the MTP-PMSG [34].

The centralized control architecture, as shown in Fig. 1(a), utilizes one central controller to control multiple converters. The VSD control method is usually adopted in the centralized control architecture to realize decoupling control [10], [12]. The research on the centralized control architecture for multiple three-phase motors primarily focuses on areas such as harmonic suppression of stator current [30], [33], fault-tolerant control [31], power-sharing between winding sets [10], sensorless control [29], and so on. Thanks to the decoupling of torque and harmonic planes realized by the VSD method, achieving harmonic suppression and sensorless control is easier compared with distributed control [29], [33]. However, the implementation of power-sharing between winding sets and fault-tolerant control may be more complex. The implementation of power-sharing in the centralized control architecture requires imposing appropriate fundamental frequency currents into the x-y harmonic planes [10], which is relatively complex. Additionally, due to the importance and uniqueness of the central controller, the failure of the central controller will shut down the whole system [13]. This limitation restricts the full utilization of the redundancy of the MTP-PMSG topology, which seriously affects the reliability of the system.

The conventional distributed control architecture with interconnected communication cables, as shown in Fig. 1(b), employs multiple controllers to control multiple inverters. In this architecture, the multi-dq modeling method is usually adopted, which is inherently superior to the centralized control architecture regarding redundancy and power-sharing [14]. The research on distributed control architecture mainly includes the decoupling method [25], the torque control method [35], and the power-sharing method [14], [34], which have excellent control performance. However, the method described earlier must require interconnected communication cables to exchange real-time information between multiple controllers for decoupling control and harmonic suppression. In addition, the controllers of MTP-PMSG also need interconnected communication cables to transmit the position signal from the only encoder installed on the motor shaft for park transformation. Even if conventional sensorless control is adopted, interconnected communication cables are also required, especially under the condition of power unbalance [26]. However, interconnected communication cables have a high probability of communication failure in the harsh operating environment of offshore wind power [15], [16]. This interconnected communication cable communication failure will break the decoupling control and the transmission of position signals between controllers of conventional distributed control architecture, and also restricts the high redundancy of the MTP-PMSG topology. Therefore, it is necessary to study a distributed control architecture that does not need interconnected communication cables between distributed controllers of the offshore wind power generation system.

To solve the problem of communication failure of interconnected communication cables under the conventional distributed control architecture of offshore wind power generation systems, this article proposes an enhanced distributed control (EDC) architecture of MTP-PMSG without interconnected communication cables. By analyzing the voltage equation of MTP-PMSG, the variation law of the equivalent inductance of the winding sets is obtained, and the decoupling mathematical model of MTP-PMSG based on the multi-dq modeling method in the EDC architecture without interconnections is derived. In addition, the encoder position signal cannot be transmitted between controllers as the lack of interconnection cables, therefore, this article proposes an enhanced distributed sensorless control (EDSC) strategy based on the proposed EDC architecture to achieve sensorless control. At the same time, considering the complicated harmonic electromagnetic coupling, a model-free

predictive harmonic current (MFPHC) suppression control strategy based on the EDC architecture is given to solve the coupling of the harmonic model and achieve harmonic suppression.

The rest of this article is organized as follows. The mathematical model of MTP-PMSG in the EDC architecture is derived in Section II. The EDSC strategy and MFPHC suppression control strategy based on the EDC architecture are proposed in Sections III and IV. A set of comparative simulations and experiments on the dual three-phase PMSG (DTP-PMSG) platform verify the validity of the proposed EDC architecture in Section V. Finally, Section VI concludes the article.

II. Mathematical Model of MTP-PMSG Under Distributed Architecture

A. Conventional Mathematical Model of MTP-PMSG

Assuming that the reluctance of stator and rotor cores, eddy current, and hysteresis losses are ignored, the voltage equation of MTP-PMSG based on the multi-dq modeling method can be expressed as follows [19]:

$$u_{di} = Ri_{di} + L_d\frac{di_{di}}{dt} - \omega L_q i_{qi} + u_{d\_coup} \tag{1}$$

$$u_{qi} = Ri_{qi} + L_q\frac{di_{qi}}{dt} + \omega L_d i_{di} + \omega\psi_f + u_{q\_coup} \tag{2}$$

$$u_{d\_coup} = \sum_{k=1,k\neq i}^{k=N}\left(L_{md}\frac{di_{dk}}{dt} - \omega L_{mq} i_{qk}\right) \tag{3}$$

$$u_{q\_coup} = \sum_{k=1,k\neq i}^{k=N}\left(L_{mq}\frac{di_{qk}}{dt} + \omega L_{md} i_{dk}\right) \tag{4}$$

where u_{di}, u_{qi} and i_{di}, i_{qi}, i_{dk}, i_{qk} are the dq-axis voltages and currents, and subscripts "i" and "k" represent the variables of the ith winding set and the kth winding set of MTP-PMSG, respectively. L_d, L_q, L_{md}, and L_{mq} are the motor self-inductances and mutual inductances, R is the stator resistance, ψ_{f} is the permanent magnet flux linkage, ω is the electrical speed, and N is the number of three-phase winding sets of MTP-PMSG.

B. Proposed Mathematical Model of MTP-PMSG

From (1) to (4), it can be seen that the stator voltage equation of one winding set is coupled with the current of other winding sets through mutual inductances. To obtain better control performance, the external interconnected communication cables between distributed controllers are usually used to interact with current information for decoupling. However, the interconnected communication cables will reduce the redundancy of the MTP-PMSG topology. Therefore, how to realize the decoupling control without a communication cable is the first problem to be solved.

The magnetic field coupling of MTP-PMSG winding sets is similar to the transformer's windings. The mathematical model of MTP-PMSG in EDC architecture can be established by imitating the transformer's mathematical equivalent circuit analysis method [17]. By substituting the equivalent transformation $i_{dk} = i_{di} \times (i_{dk}/i_{di})$and $i_{qk} = i_{qi} \times (i_{qk}/i_{qi})$ into the voltage (1) and (2), the coupling term of the other winding sets can be expressed by the ith winding set variables, and (1) and (2) can be rewritten as follows:

$$\begin{aligned} u_{di} = {} & Ri_{di} + \left(L_d + \sum_{k=1,k\neq i}^{k=N} L_{md}\frac{i_{dk}}{i_{di}}\right)\frac{di_{di}}{dt} \\ & - \omega\left(L_q + \sum_{k=1,k\neq i}^{k=N} L_{mq}\frac{i_{qk}}{i_{qi}}\right) i_{qi} \\ & + i_{di} d\left(\sum_{k=1,k\neq i}^{k=N} L_{md}\frac{i_{dk}}{i_{di}}\right)/dt \end{aligned} \tag{5}$$

$$\begin{aligned} u_{qi} = {} & Ri_{qi} + \left(L_q + \sum_{k=1,k\neq i}^{k=N} L_{mq}\frac{i_{qk}}{i_{qi}}\right)\frac{di_{qi}}{dt} + \omega\psi_f \\ & + \omega\left(L_d + \sum_{k=1,k\neq i}^{k=N} L_{md}\frac{i_{dk}}{i_{di}}\right) i_{di} \\ & + i_{qi} d\left(\sum_{k=1,k\neq i}^{k=N} L_{mq}\frac{i_{qk}}{i_{qi}}\right)/dt. \end{aligned} \tag{6}$$

For analysis simplification, defining the K_{di} and K_{qi} as follows:

$$K_{di} = \sum_{k=1,k\neq i}^{k=N}\frac{i_{dk}}{i_{di}}S_k, K_{qi} = \sum_{k=1,k\neq i}^{k=N}\frac{i_{qk}}{i_{qi}}S_k \tag{7}$$

where K_{di} and K_{qi} are the total current ratios, representing the sum of the current ratios of the ith winding set to the rest N-1 winding sets in dq-axis. S_k represents the health status of the kth winding set, and S_k equals 1 or 0, indicating that the kth winding set is normal or faulty. Substituting (7) into (5) and (6)

$$u_{di} = Ri_{di} + L_{e\_di}\frac{di_{di}}{dt} - \omega L_{e\_qi} i_{qi} + i_{di} L_{md}\frac{dK_{di}}{dt} \tag{8}$$

$$u_{qi} = Ri_{qi} + L_{e\_qi}\frac{di_{qi}}{dt} + \omega L_{e\_di} i_{di} + \omega\psi_f + i_{qi} L_{mq}\frac{dK_{qi}}{dt} \tag{9}$$

where L_{e_di} and L_{e_qi} are the equivalent inductance after converting the other winding sets information to the ith winding set. L_{e_di} and L_{e_qi} can be expressed as follows:

$$\begin{aligned} L_{e\_di} &= L_d + K_{di} L_{md} \\ L_{e\_qi} &= L_q + K_{qi} L_{mq}. \end{aligned} \tag{10}$$

It can be seen from (8) and (9) that the stator voltage equation of the ith winding set does not explicitly contain the coupling term of the other winding sets, and the coupling terms are replaced by the total current ratio between the winding sets.

The equivalent inductance of each set of windings will change with K_{di} and K_{qi}. Taking the q-axis inductance of the first

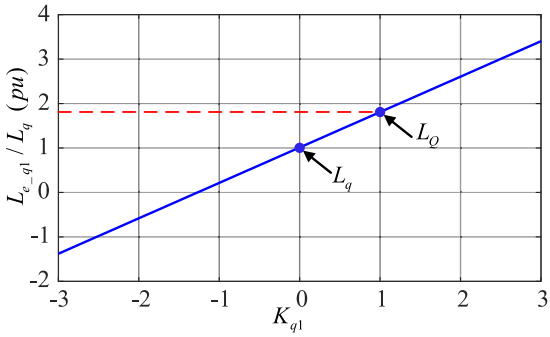

Fig. 2. Relationship between equivalent inductance and total current ratio.

winding sets of DTP-PMSG as an example, the relationship between the q-axis equivalent inductance and the total current ratio is shown in Fig. 2. The following conclusions can be obtained.

1) When the current/power of the two winding sets is unbalanced, the equivalent inductance would change with the change of the total current ratio.
2) When $K_{q1} = 0$, the second winding set is equivalent to a nonoperating state or open-phase fault state. At this time, the health status S_k is 0, and the DTP-PMSG is equivalent to the conventional three-phase PMSG. The equivalent inductance is $L_{e\_q1} = L_q$.
3) When $K_{q1} = 1$, the q-axis currents of the two sets of windings are balanced. Then, the mathematical model under the proposed EDC architecture is equivalent to the mathematical model under the VSD method, and $L_{e\_q1} = L_Q$, where L_Q is the q-axis inductance of DTP-PMSG under the VSD method [19].
4) Specifically, when $i_{q1} = i_{q2} = 0$, the K_{q1} is defined as 1. When $i_{q1} = 0$ $i_{q2} \neq 0$, the K_{q1} is defined as a relatively large number, which can be taken as 100 in practical applications.

The voltage (8) and (9) of stator winding have been transformed into a form similar to conventional motors. The only difference is that the MTP-PMSG contain differential disturbance term ($i_{di}L_{md}\frac{dK_{di}}{dt}$ and $i_{qi}L_{mq}\frac{dK_{qi}}{dt}$). When the MTP-PMSG works in a steady state, the influence of this differential term is very small. In addition, due to the low requirement of dynamic response in the offshore wind power generation system, the differential disturbance term of the dq-axis accounts for a small proportion and can be ignored. Therefore, each set of windings can be equivalent to a conventional three-phase PMSG in the wind power generation system with low dynamic requirements. The main control and modulation algorithm of conventional three-phase PMSG can be applied to MTP-PMSG based on the proposed EDC architecture. However, the failure of the interconnected communication cables will cause the failure of the conventional position sensor/sensorless control algorithm and affect the performance of harmonic suppression analyzed in Section I. To address these challenges, the EDSC strategy and MFPHC suppression control strategy based on the proposed EDC architecture are given in Sections III and IV.

III. EDSC Based on Extended Back EMF in EDC Architecture

In the offshore PMSG system, the position sensor may fail in the high salt and high humidity environment. In addition, under the multiphase motor conventional distributed control architecture, it is inevitable to add interconnected communication cables between multiple controllers to share the position sensor information, which reduces the reliability and anti-interference ability of the system. Therefore, an EDSC method based on extended back electromotive force (EMF) under the EDC architecture is proposed in this section.

A. Extended Back EMF Model in EDC Architecture

Through the inverse Park transformation matrix [20], the mathematical model in (8) and (9) is transformed into the static $\alpha\beta$ coordinate, which can be expressed as follows:

$$\begin{cases} u_{\alpha i} = Ri_{\alpha i} + L_{e\_di}\frac{di_{\alpha i}}{dt} + \omega(L_{e\_di} - L_{e\_qi})i_{\beta i} \\ \quad + i_{\alpha i}L_{md}\frac{dK_{di}}{dt} + E_{\alpha i} \\ u_{\beta i} = Ri_{\beta i} + L_{e\_di}\frac{di_{\beta i}}{dt} - \omega(L_{e\_di} - L_{e\_qi})i_{\alpha i} \\ \quad + i_{\beta i}L_{mq}\frac{dK_{qi}}{dt} + E_{\beta i} \end{cases} \tag{11}$$

$$\begin{cases} E_{\alpha i} = -\left((L_{e\_di} - L_{e\_qi})\left(\omega i_{di} - \frac{di_{qi}}{dt}\right) + \omega\psi_f\right)\sin\theta_i \\ E_{\beta i} = \left((L_{e\_di} - L_{e\_qi})\left(\omega i_{di} - \frac{di_{qi}}{dt}\right) + \omega\psi_f\right)\cos\theta_i \end{cases} \tag{12}$$

where $u_{\alpha i}$, $u_{\beta i}$, $i_{\alpha i}$, $i_{\beta i}$ are the stator voltage and current in the static $\alpha\beta$ coordinate, $E_{\alpha i}$ and $E_{\beta i}$ are the extended back EMF in the static $\alpha\beta$ coordinate, and θ_i is the rotor position angle.

Equation (11) contains the $i_{\alpha i}L_{md}\frac{dK_{di}}{dt}$ and $i_{\beta i}L_{mq}\frac{dK_{qi}}{dt}$, which is different from the conventional three-phase PMSG. If K_{di} and K_{qi} have random noise or step change, the classical differentiator will amplify the noise. To extract the differential signal, the tracking differentiator (TD) is introduced to obtain a smooth differential signal in noise or step change occasions. According to Han's definition of TD [21], the state equation of TD can be expressed as follows:

$$\begin{cases} \dot{x}_1 = x_2 \\ \dot{x}_2 = -r\text{sign}\left(x_1 - v(t) + \frac{x_2|x_2|}{2r}\right) \end{cases} \tag{13}$$

where x_1 and x_2 are the state variables representing the total current ratio and the differential of the total current ratio, r is the convergence factor, and $v(t)$ represents the input reference value of the total current ratio. The detailed derivation and proof process of TD have been given by [21]. Due to the length of the article, it will not be explained in detail here.

B. Extended Back EMF Observer

In (12), the extended back EMF includes the rotor position and the speed of the MTP-PMSG under the EDC architecture. Only when the extended back EMF is accurately obtained, can the speed and position information of the motor be calculated. According to (11), the extended back EMF observer is constructed

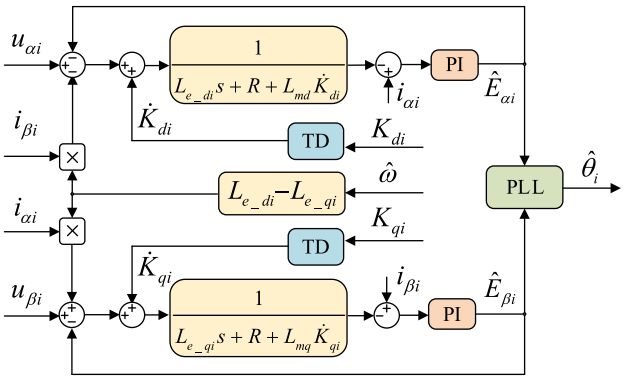

Fig. 3. EDSC method block diagram based on extended back EMF in EDC architecture.

as follows:

$$\begin{cases} u_{\alpha i} = R\hat{i}_{\alpha i} + \hat{i}_{\alpha i}L_{md}\frac{dK_{di}}{dt} + L_{e\_di}\frac{d\hat{i}_{\alpha i}}{dt} \\ + \hat{\omega}(L_{e\_di} - L_{e\_qi})i_{\beta i} + \hat{E}_{\alpha i} \\ u_{\beta i} = R\hat{i}_{\beta i} + \hat{i}_{\beta i}L_{mq}\frac{dK_{qi}}{dt} + L_{e\_qi}\frac{d\hat{i}_{\beta i}}{dt} \\ - \hat{\omega}(L_{e\_di} - L_{e\_qi})i_{\alpha i} + \hat{E}_{\beta i} \end{cases} \tag{14}$$

where $\hat{i}_{\alpha i}$ and $\hat{i}_{\beta i}$ are the estimated stator current in the static $\alpha\beta$ coordinate. Then $\hat{E}_{\alpha i}$ and $\hat{E}_{\beta i}$ are the estimated extended back EMF in the static $\alpha\beta$ coordinate, expressed as follows:

$$\begin{cases} \hat{E}_{\alpha i} = \left(k_P + \frac{k_I}{s}\right)\left(i_{\alpha i} - \hat{i}_{\alpha i}\right) \\ \hat{E}_{\beta i} = \left(k_P + \frac{k_I}{s}\right)\left(i_{\beta i} - \hat{i}_{\beta i}\right) \end{cases} \tag{15}$$

where k_P and k_I are the proportional and integral gains of the PI controller. After obtaining the estimated extended back EMF, the estimated rotor position $\hat{\theta}_i$ could be extracted from the phase of the estimated extended back EMF using the phase-locked loop (PLL) [22]. According to (13)–(15), the extended back EMF observer under the EDC architecture is shown in Fig. 3.

IV. Current Harmonic Suppression of MTP-PMSG in EDC Architecture

Compared with the conventional three-phase PMSG, the current harmonic problem of MTP-PMSG is more prominent. For example, DTP-PMSG has a lower $6\,\mathrm{k} \pm 1$ $(k = 1, 3, 5\ldots)$ order harmonic impedance, so a small harmonic voltage will cause a larger current harmonic [20]. At the same time, by deducing the harmonic mathematical model of multiple three-phase motors in the distributed control architecture, it is found that there is electromagnetic coupling between winding sets in the harmonic model. In the wind power system, the harmonic suppression performance will be limited in case of the failure of the interconnection communication cables between the distributed controllers. Thus, in this section, an MFPHC suppression control method is proposed, which can effectively suppress harmonics notwithstanding whether the output power and current of the winding sets are balanced or unbalanced.

A. Analysis of MTP-PMSG Harmonic Model

In the natural coordinate reference system, the stator harmonic current of MTP-PMSG can be expressed as follows [38]:

$$\begin{cases} i_{Aij} = I_{ij}\cos(j(\omega t - (i-1)\delta_m) + \theta_{ij}) \\ i_{Bij} = I_{ij}\cos(j(\omega t - 2\pi/3 - (i-1)\delta_m) + \theta_{ij}) \\ i_{Cij} = I_{ij}\cos(j(\omega t + 2\pi/3 - (i-1)\delta_m) + \theta_{ij}) \\ j = 1, 5, 7, 11, 13\ldots \end{cases} \tag{16}$$

where i_{Aij}, i_{Bij}, i_{Cij} are the stator phase currents of winding sets, I_{ij} is phase current amplitudes, δ_m is the angle of phase difference between winding sets, θ_{ij} is the initial angles of phase currents, and j represents harmonic order. Taking the fifth harmonic as an example, the harmonic model of MTP-PMSG is derived as follows.

In the fundamental multi-dq coordinate, the fifth harmonic current can be expressed as follows:

$$\begin{cases} i^1_{di5} = I_{i5}\cos(-6\omega t + \theta_{i5}) \\ i^1_{qi5} = I_{i5}\sin(-6\omega t + \theta_{i5}) \end{cases} \tag{17}$$

where i^1_{di5}, i^1_{qi5} are the fifth harmonic current components of ith winding set in the fundamental multi-dq coordinate. According to (17), the fifth stator voltage harmonic equation of the ith winding set can be written as follows:

$$\begin{cases} u^1_{di5} = Ri^1_{di5} + L_d\frac{di^1_{di5}}{dt} - \omega L_q i^1_{qi5} \\ + \sum_{k=1,k\neq i}^{k=N}\left(L_{md}\frac{di^1_{dk5}}{dt} - \omega L_{mq}i^1_{qk5}\right) \\ u^1_{qi5} = Ri^1_{qi5} + L_q\frac{di^1_{qi5}}{dt} + \omega L_d i^1_{di5} \\ + \sum_{k=1,k\neq i}^{k=N}\left(L_{mq}\frac{di^1_{qk5}}{dt} - \omega L_{md}i^1_{dk5}\right) \end{cases} \tag{18}$$

where u^1_{di5} and u^1_{qi5} are the fifth harmonic components of voltage in the fundamental multi-dq coordinate, i^1_{dk5}, i^1_{qk5} are the fifth harmonic current components of kth winding set in the fundamental multi-dq coordinate. By using the Park transformation, in which the transform angle is 6ω, (18) can be transformed from the fundamental multi-dq coordinate into the fifth-order multi-dq coordinate and expressed as follows:

$$\begin{cases} u^5_{di5} = Ri^5_{di5} + L_d\frac{di^5_{di5}}{dt} + 5\omega L_q i^5_{qi5} \\ + \sum_{k=1,k\neq i}^{k=N}\left(L_{md}\frac{di^5_{dk5}}{dt} + 5\omega L_{mq}i^5_{qk5}\right) \\ u^5_{qi5} = Ri^5_{qi5} + L_q\frac{di^5_{qi5}}{dt} - 5\omega L_d i^5_{di5} \\ + \sum_{k=1,k\neq i}^{k=N}\left(L_{mq}\frac{di^5_{qk5}}{dt} - 5\omega L_{md}i^5_{dk5}\right) \end{cases} \tag{19}$$

where u^5_{di5}, u^5_{qi5} and i^5_{di5}, i^5_{qi5}, i^5_{dk5}, i^5_{qk5} are the fifth voltage and current harmonic components in the fifth-order multi-dq coordinate, respectively, and the fifth current harmonic components can be expressed as follows:

$$\begin{cases} i^5_{di5} = I_{i5}\cos\theta_{i5} \\ i^5_{qi5} = I_{i5}\sin\theta_{i5} \end{cases}. \tag{20}$$

It can be seen from (19) that the harmonic voltage equation of the ith winding set is related to its variables and coupled with the harmonic current components of the other winding sets. In the distributed control architecture without interconnected communication cables, the decoupling control cannot be carried out, and

it is difficult to obtain a satisfactory harmonic suppression effect. Therefore, this article proposes an MFPHC suppression control method, which can suppress harmonic in the EDC architecture without interconnected communication cables.

B. MFPHC Control

For a single-input single-output nonlinear system, the input and output signals of the system can be used to establish an ultralocal model [23], which is expressed as follows:

$$\dot{y} = F + \alpha u \tag{21}$$

where u and y are the input and output of the system, respectively, α is the designed system state gain factor, and F represents the known and unknown parts of the system. According to (21), the model-free control law is designed as follows:

$$u = (-\hat{F} + \dot{y}^* + \xi)/\alpha \tag{22}$$

where $\hat{F}$ represents the estimated value of F, y^* is the output reference value, and ξ is the designed controller, which is designed as a proportional controller, expressed as follows:

$$u = (-\hat{F} + \dot{y}^* + K_p e)/\alpha \tag{23}$$

where $e = y^* - y$, and K_p is the proportional controller coefficient.

Based on the harmonic model of MTP-PMSG, the fifth harmonic ultralocal model is established in (19) and (21), which is expressed as follows:

$$\begin{cases} \frac{di^5_{di5}}{dt} = F^5_{di5} + \alpha^5_{di5} u^5_{di5} \\ \frac{di^5_{qi5}}{dt} = F^5_{qi5} + \alpha^5_{qi5} u^5_{qi5} \end{cases} \tag{24}$$

where F^5_{di5}, F^5_{qi5} and α^5_{di5}, α^5_{qi5} represent the unknown part and state gain factor, respectively, in the fifth-order multi-dq coordinate.

Based on the differential algebra method [24], the input and output of the system are used to estimate $\hat{F}$, which can be expressed as follows:

$$\hat{F} = -\frac{3!}{T^3}\int_0^T \left((T-2\sigma)y(\sigma) + \alpha\sigma(T-\sigma)u(\sigma)\right) d\sigma \tag{25}$$

where $T = nT_s$, n is the number of control periods, T_s is the control period, and the superscript "$\wedge$" represents the estimated value of the variable. By using the gradient integral method [24] to solve (25), the discrete-time domain expression of $\hat{F}$ is

$$\hat{F} = -\frac{3}{n^3 T_s}\sum_{m=1}^{n} \begin{array}{l} ((n-2(m-1)) \times y[m-1] + \\ \alpha(m-1)T_s(n-(m-1)) \\ \times u[m-1] + \\ (n-2m) \times y[m] \\ +\alpha m T_s (n-m) \times u[m]) \end{array} . \tag{26}$$

According to (23) and (26), the MFPHC controller in the fifth-order multi-dq coordinate of the ith winding set of MTP-PMSG is designed as follows:

$$\begin{cases} u^{5*}_{di5} = \frac{-\hat{F}^5_{di5} + di^{5*}_{di5}/dt + K^5_{pdi5}(i^{5*}_{di5} - i^5_{di5})}{\alpha^5_{di5}} \\ u^{5*}_{qi5} = \frac{-\hat{F}^5_{qi5} + di^{5*}_{qi5}/dt + K^5_{pqi5}(i^{5*}_{qi5} - i^5_{qi5})}{\alpha^5_{qi5}} \end{cases} \tag{27}$$

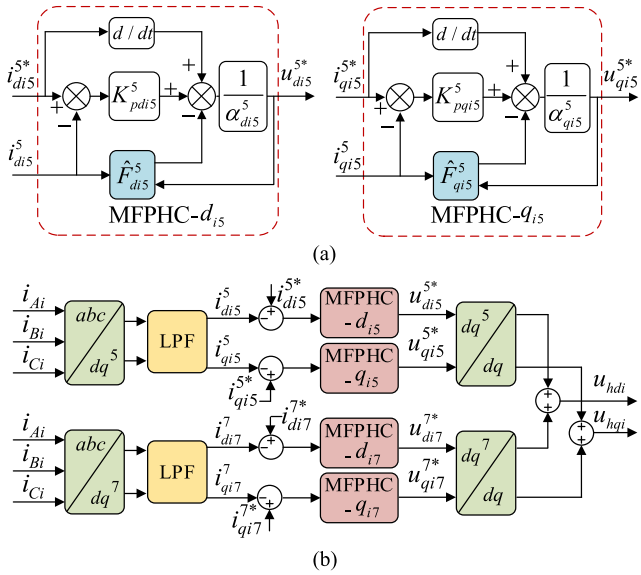

Fig. 4. Block diagram of MFPHC control method. (a) MFPHC controller. (b) Block diagram of fifth and seventh harmonic suppression based on MFPHC controller in EDC architecture.

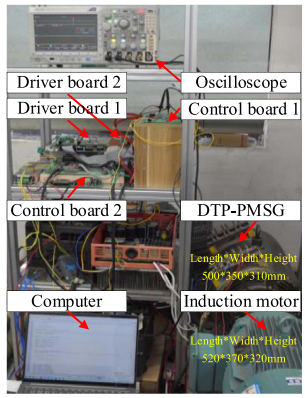

Fig. 5. Experiment platform for the DTP-PMSG.

$$\begin{cases} \hat{F}^5_{di5} = \frac{-3}{n^3 T_s}\sum_{m=1}^{n} \begin{array}{l} ((n-2(m-1)) \times i^5_{di5}[m-1] + \\ \alpha^5_{di5}(m-1)T_s(n-(m-1)) \\ \times u^{5*}_{di5}[m-1] + \\ (n-2m) \times i^5_{di5}[m] \\ + \alpha^5_{di5} m T_s (n-m) \times u^{5*}_{di5}[m]) \end{array} \\ \hat{F}^5_{qi5} = \frac{-3}{n^3 T_s}\sum_{m=1}^{n} \begin{array}{l} ((n-2(m-1)) \times i^5_{qi5}[m-1] + \\ \alpha^5_{qi5}(m-1)T_s(n-(m-1)) \\ \times u^{5*}_{qi5}[m-1] + \\ (n-2m) \times i^5_{qi5}[m] + \alpha^5_{qi5} m T_s \\ (n-m) \times u^{5*}_{qi5}[m]) \end{array} \end{cases} \tag{28}$$

where the superscript "$*$" represents the reference value of the variables, K^5_{pdi5}, K^5_{pqi5} and $\hat{F}^5_{di5}$, $\hat{F}^5_{qi5}$ are the proportional controller coefficient and the estimated value of the unknown part in fifth-order multi-dq coordinate, respectively.

According to (27) and (28), the MFPHC controller of MTP-PMSG in fifth-order multi-dq coordinate is shown in Fig. 4(a) .

TABLE I
PARAMETERS OF DTP-PMSG

Parameter	Value
Stator resistance R	1.89 Ω
d-axis inductances L_d	0.0216 H
q-axis inductances L_q	0.0367 H
Mutual inductances L_{md}	0.0203 H
Mutual inductances L_{mq}	0.0354 H
Permanent magnet flux linkage	0.92 Wb
Pole pairs	5

Taking the fifth and seventh harmonics as an example, Fig. 4(b) shows the block diagram of the MFPHC control method in EDC architecture. In Fig. 4(b), the fifth harmonic current in fifth-order multi-dq coordinate and the seventh harmonic current in seventh-order multi-dq coordinate can be obtained, respectively, using coordinate transformation and first-order low-pass filters (LPFs). The LPFs can be used to filter the components of other frequencies while retaining the dc components. The cut-off frequency of LPF needs to be tuned in the experiment to trade-off the filtering performance and dynamic performance [27]. The MFPHC controller shown in Fig. 4(a) is used to calculate the voltage harmonic compensation, and then the voltage harmonic compensation will be transformed into the fundamental multi-dq coordinate.

V. Simulation and Experimental Results

A. Experimental System

To verify the effectiveness of the proposed EDC architecture without interconnected communication cables, a 7.5 kW DTP-PMSG is selected as the test motor. The DTP-PMSG distributed control platform is built as shown in Fig. 5. The parameters of the DTP-PMSG are listed in Table I. The DTP-PMSG is coaxially connected with a 7.5 kW conventional three-phase induction motor (rated voltage/current 380 V/17.8 A), which serves as a prime mover. The proposed EDC architecture method algorithm is implemented on two control boards without interconnected communication cables, and the digital signal processor TMS320F28377 is used to execute the proposed method. The PWM signal is generated by a field programmable gate array (FPGA). The incremental encoder with a 2048 pulse is used to detect the precise position and speed of the rotor for comparison with the experimental results of the proposed EDC architecture method.

The initial reference command of this wind power generation system is the power reference of the transmission system operator shown in Fig. 6(a). The subscript "1" and "2" refer to the variables of the two winding sets of DTP-PMSG, and the superscript "$*$" refers to the given value. The power balance sharing mode or the optimal converter efficiency strategy mode proposed in [18] can be chosen to obtain the torque reference command of each set of windings. The power balance sharing mode means that the power command of each set of windings is equal, while the optimal converter efficiency strategy mode means the power command of each winding sets is adjusted according to the power requirements to achieve the overall

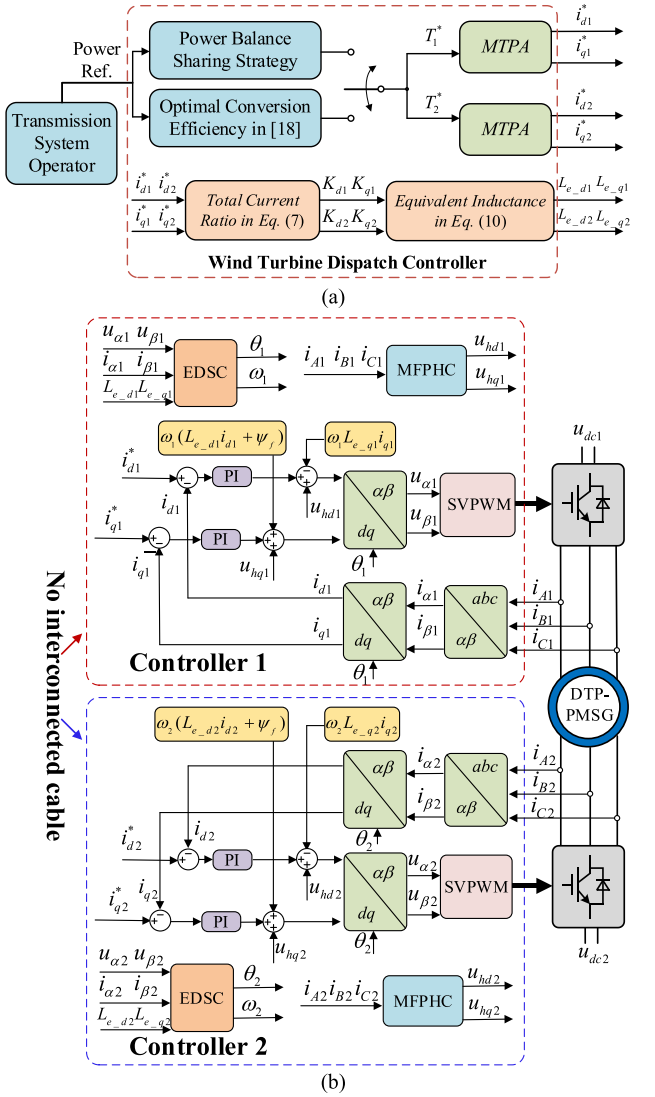

Fig. 6. Proposed drive system. (a) Wind turbine dispatch controller block. (b) Control diagram of the proposed EDC architecture for the DTP-PMSG.

optimal efficiency output of the converter system [18]. After obtaining the torque command, the maximum torque per ampere (MTPA) method [28] is used to calculate the current reference command in the dq-axis. However, in this article, in order to verify the applicability of the proposed EDC architecture, the current command will be directly given within the rated range in the following experiments without using this optimal converter efficiency strategy. The equivalent inductance is obtained according to the current command and (7) and (10).

Fig. 6(b) shows the control diagram of the proposed EDC architecture for DTP-PMSG. The controller of each winding of DTP-PMSG operates independently without mutual influence, which increases the redundancy of the system and is easy to be extended to the operation control of other MTP-PMSGs. Fig. 3 shows the block diagram of the EDSC module, in which the estimated rotor positions $\hat{\theta}_1$ and $\hat{\theta}_2$ are calculated by their respective controllers to achieve sensorless control under current balanced or unbalanced conditions in EDC architecture. Fig. 4

shows the block diagram of the MFPHC control module, and the 5th, 7th, 17th, and 19th order current harmonic are selected to be suppressed. The harmonic voltage compensations u_{hdq1} and u_{hdq2}, calculated by the MFPHC controller are added to the fundamental voltage to suppress the selected harmonics.

B. Simulation Results

Before experimental verification, the DTP-PMSG drive system and the proposed EDC architecture method are modeled and simulated using the MATLAB/Simulink environment. The motor parameters used in the simulation are presented in Table I. The simulation results of the proposed method for both steady-state and dynamic operation of the DTP-PMSG are presented to demonstrate its operational performance under power balance and power unbalance conditions.

Fig. 7 shows the comparison simulation results of the steady-state operation between the conventional distributed control and the proposed EDC method under power balance conditions. The motor speed is set to 200 rpm, and the given reference q-axis currents of two winding sets are $i_{q1}^{*} = i_{q2}^{*} = 10$ A, with the given currents for the d-axis being set to 0 A. From Fig. 7(b), it is evident that based on the proposed EDC method, the phase current harmonic of DTP-PMSG is very small, with a THD of 3.92%. Additionally, the torque waveform is smoother and more stable than the conventional distributed control method. These results demonstrate that the MFPHC method based on the proposed EDC architecture can effectively suppress harmonics. The rotor position information in Fig. 7(b) indicates that the position errors between the estimated rotor position using the proposed EDSC method and the actual rotor position angle are within 5°, demonstrating the effectiveness of the proposed EDSC method under steady-state conditions.

In Fig. 8, the simulation results of the proposed method under power balance conditions during dynamic operation are presented. The given reference q-axis currents of the two winding sets are $i_{q1}^{*} = i_{q2}^{*} = 5$ A within the first 0–0.4 s, then increasing to $i_{q1}^{*} = i_{q2}^{*} = 10$ A within the next 0.4–1.4 s, and then decreasing back to $i_{q1}^{*} = i_{q2}^{*} = 5$ A after 1.4 s. It is evident from Fig. 8 that the proposed method effectively ensures that both windings of the DTP-PMSG can rapidly follow the given current command, and the torque waveform remains stable throughout the dynamic process. Additionally, the proposed EDSC method can promptly converge and estimate the rotor positions of both sets of windings during dynamic processes, with a maximum error of no more than 10°.

To verify the power-sharing performance of the proposed method, the simulation results of the proposed method under power unbalance conditions are presented in Fig. 9. The given reference q-axis currents of two winding sets under power-sharing conditions are shown in Table II, and the sum of the given reference current values of the two winding sets is 20 A. Fig. 9 demonstrates that the proposed EDC method can effectively track the given current value and achieve power-sharing between the two sets of windings even under a wide range of power unbalance conditions, with current ratios of the two sets of windings ranging from 1/9 to 9. The estimated rotor position shown in Fig. 9 fluctuates slightly during the power-sharing process, and the rotor position error values are within 5°, proving that the proposed EDSC method exhibits excellent performance in the power-sharing condition.

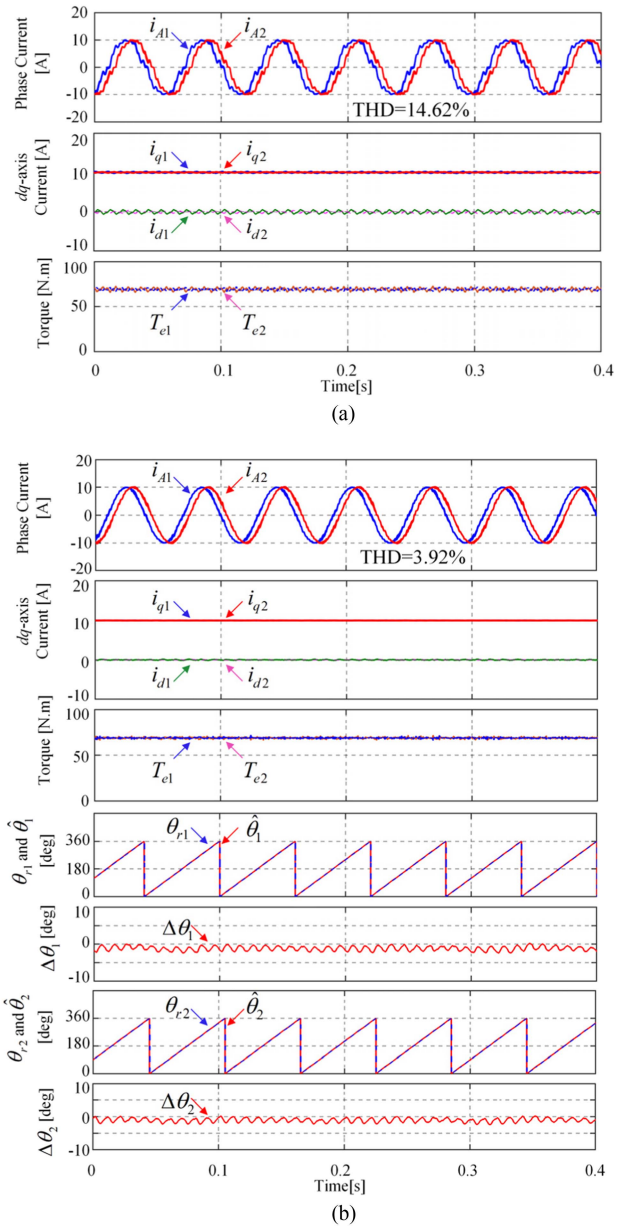

Fig. 7. Comparison simulation results between the conventional distributed control and the proposed EDC architecture method under power balance steady-state operation. (a) Conventional distributed control. (b) Proposed EDC method.

TABLE II
GIVEN REFERENCE CURRENTS AND CURRENT RATIO OF DTP-PMSG UNDER CURRENT UNBALANCE

Time[s]	0-0.2	0.2-0.6	0.6-1.0	1.0-1.4	1.4-1.8	1.8-2.0
i_{q1}[A]	10	5	2	15	18	10
i_{q2}[A]	10	15	18	5	2	10
K_{q1}	1	3	9	1/3	1/9	1

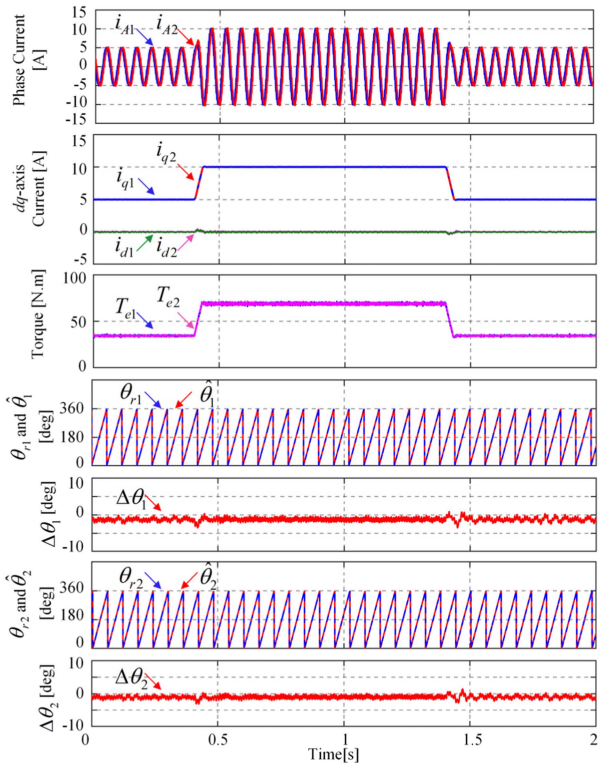

Fig. 8. Simulation results of the proposed EDC architecture method under power balance dynamic operation.

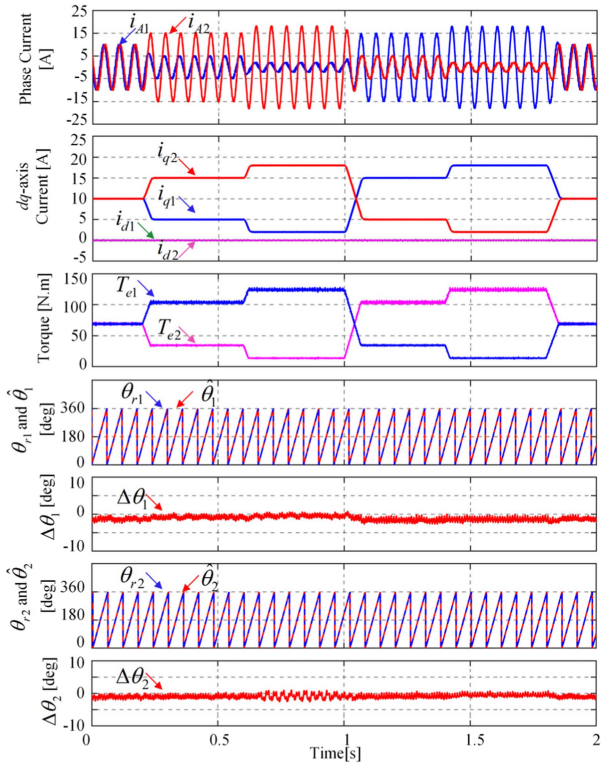

Fig. 9. Simulation results of the proposed EDC architecture method under power unbalance dynamic operation.

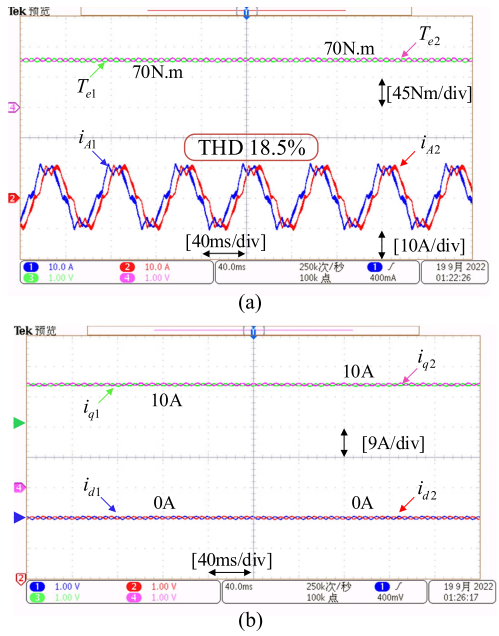

Fig. 10. Experimental results of DTP-PMSG based on conventional distributed control under current balanced steady-state operation. (a) Phase current and torque waveform. (b) dq -axis currents.

C. Experimental Results of Steady-State Operation Under Current Balance

The steady-state operation comparison experimental result of conventional distributed control with dual dq modeling method and proposed EDC architecture method under the current balance are shown in Figs. 10 and 11, respectively. The motor speed provided by the induction motor is 200 rpm, and the input given current reference values of the two winding sets of the DTP-PMSG are $i_{q1}^{*} = i_{q2}^{*} = 10$ A and $i_{d1}^{*} = i_{d2}^{*} = 0$ A. From the comparison of phase current and torque waveforms in Figs. 10(a) and 11(a) that the proposed EDC architecture method can effectively reduce stator current harmonics, which the total harmonic distortion (THD) is reduced from 18.5% to 5.2%. Meanwhile, the torque ripple under steady-state operation is also reduced. Figs. 10(b) and 11(b) show that the dq-axis currents based on the proposed EDC architecture method can better track the reference value under steady-state operation, which also verifies the MFPHC control method can suppress stator harmonic current in steady state. The actual rotor position obtained by the incremental encoder, the estimated rotor position, and the position error of the two winding sets based on the proposed method are shown in Fig. 11(c) and (d), respectively. It can be obtained that the position errors of the two winding sets are within 5°, which verifies that the proposed EDSC method in EDC architecture is effective in the steady state.

D. Experimental Results of Dynamic Operation Under Current Balance

To verify the dynamic operation performance of the proposed EDC architecture method, Fig. 12 shows the load increase and

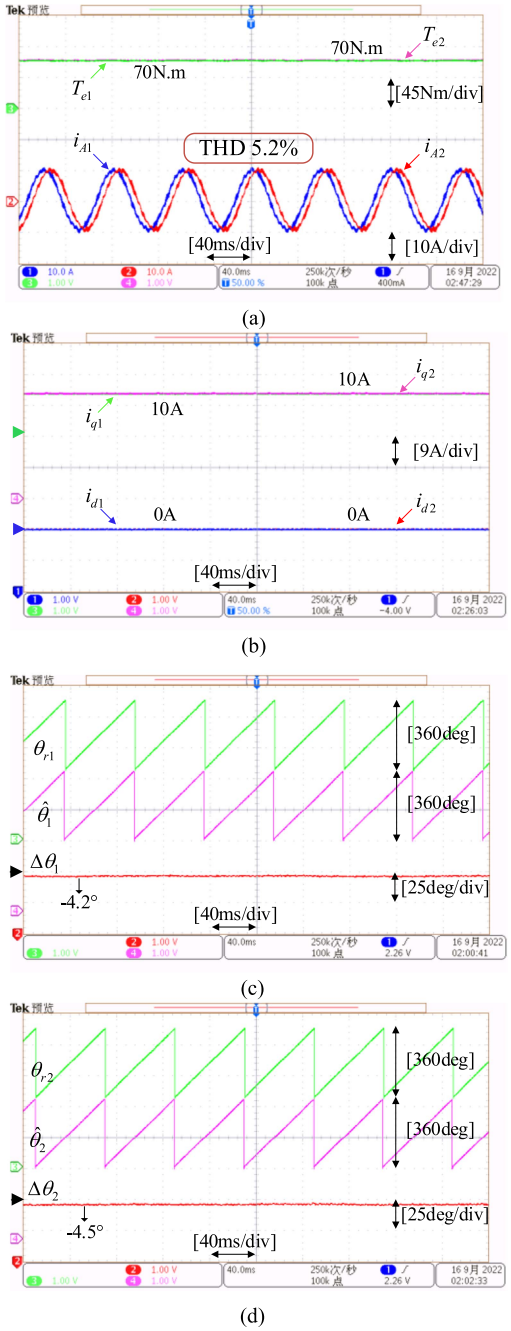

Fig. 11. Experimental results of DTP-PMSG based on proposed EDC architecture method under current balanced steady-state operation. (a) Phase current and torque waveform. (b) dq -axis currents. (c) Actual rotor position θ_{r1}, estimated rotor position $\hat{\theta}_1$, and corresponding position error $\Delta\theta_1$ of the first set of windings. (d) Actual rotor position θ_{r2}, estimated rotor position $\hat{\theta}_2$, and corresponding position error $\Delta\theta_2$ of the second set of windings.

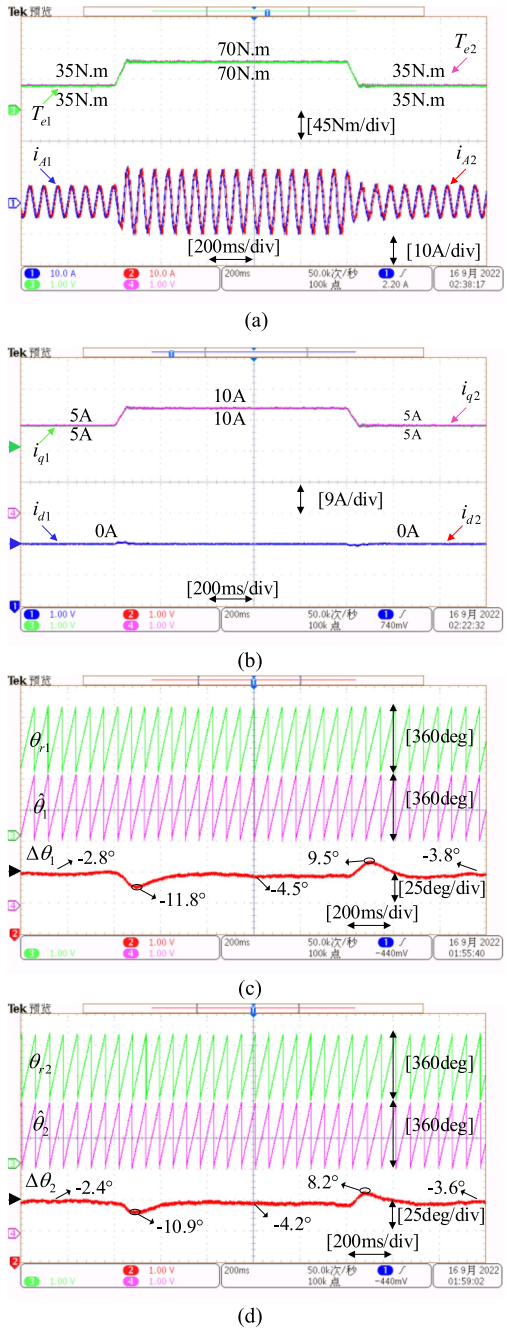

Fig. 12. Experimental results of DTP-PMSG based on proposed EDC architecture method under current balanced dynamic operation. (a) Phase current and torque waveform. (b) dq -axis currents. (c) Actual rotor position θ_{r1}, estimated rotor position $\hat{\theta}_1$, and corresponding position error $\Delta\theta_1$ of the first set of windings. (d) Actual rotor position θ_{r2}, estimated rotor position $\hat{\theta}_2$, and corresponding position error $\Delta\theta_2$ of the second set of windings.

decrease experiment results of DTP-PMSG under the current balance. The given reference q-axis currents of two winding sets are $i_{q1}^* = i_{q2}^* = 5$ A in 0–0.4 s, which are increased to $i_{q1}^* = i_{q2}^* = 10$ A in 0.4 s and decreased to $i_{q1}^* = i_{q2}^* = 5$ A in 1.4 s. The given reference d-axis currents of two winding sets are set to 0 A. It can be seen from Fig. 12(a) and (b) that the phase currents of the two winding sets are balanced, and the dq-axis currents can be accurately tracked to the given reference value. Fig. 12(c) and (d) show the estimated rotor position waveform of the two winding sets and the corresponding position error waveform with the actual rotor position values in dynamic operation. It can be seen the proposed EDSC method in EDC architecture can quickly estimate the rotor position value under the dynamic operation state, and the maximum position error is restricted within 12°.

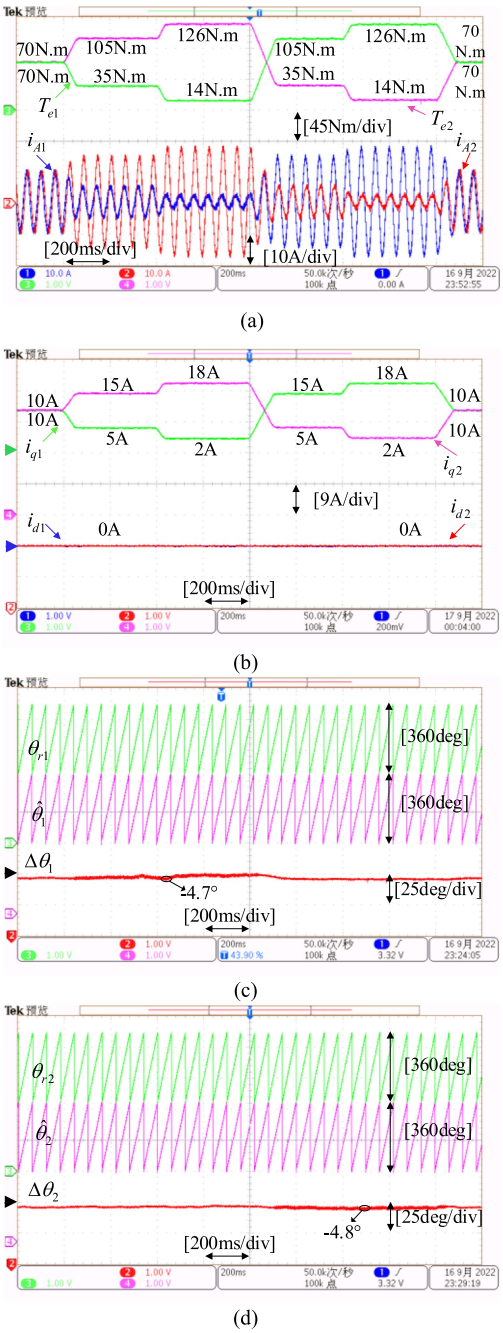

Fig. 13. Experimental results of DTP-PMSG based on proposed EDC architecture method under power and current unbalanced dynamic operation. (a) Phase current and torque waveform. (b) dq -axis currents. (c) Actual rotor position θ_{r1}, estimated rotor position $\hat{\theta}_1$, and corresponding position error $\Delta\theta_1$ of the first set of windings. (d) Actual rotor position θ_{r2}, estimated rotor position $\hat{\theta}_2$, and corresponding position error $\Delta\theta_2$ of the second set of windings.

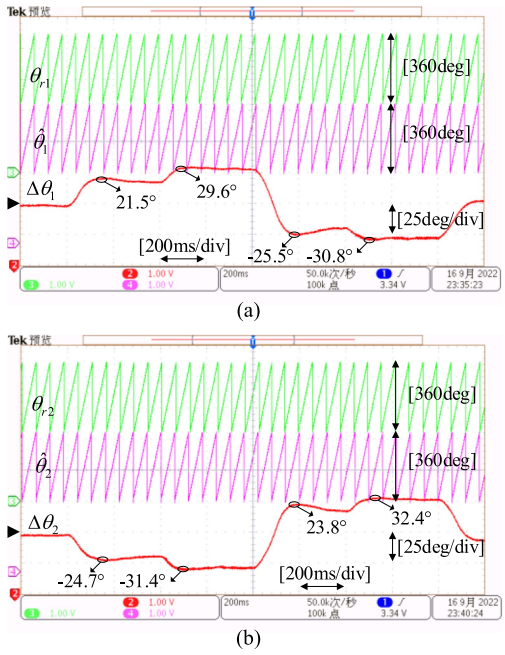

Fig. 14. Experimental results of DTP-PMSG based on conventional distributed control under power and current unbalanced dynamic operation. (a) Actual rotor position θ_{r1}, estimated rotor position $\hat{\theta}_1$, and corresponding position error $\Delta\theta_1$ of the first set of windings. (b) Actual rotor position θ_{r2}, estimated rotor position $\hat{\theta}_2$, and corresponding position error $\Delta\theta_2$ of the second set of windings.

E. Experimental Results of Dynamic Operation Under Power and Current Unbalance

To verify the operation performance of the proposed EDC architecture method under power and current unbalance, Figs. 13 and 14 show the dynamic load increase and decrease comparison experiments of the conventional distributed control and the proposed EDC architecture method of DTP-PMSG. The given reference dq-axis currents of two winding sets are shown in Table II. The current ratio of two winding sets changes with the change of the given reference current. The comparison experiments give the operation results of the current ratio from 1/9 to 9, which verify that the proposed EDC architecture method can operate effectively under the condition of extremely unbalanced power and current between two winding sets.

The stator phase current and torque of the two winding sets are shown in Fig. 13(a). It can be seen that the proposed EDC architecture method can realize the arbitrary torque/current sharing of the two winding sets under the unbalanced condition when the total output torque/current of the DTP-PMSG remains unchanged. This is of great significance for a wind turbine to realize arbitrary power-sharing of winding sets. Fig. 13(b) shows the dq-axis current values of the two winding sets. It can be seen that the q-axis current can quickly track the given reference value during the dynamic process, and there is no obvious fluctuation in the d-axis current in the dynamic process, which proves that the proposed EDC architecture method has accurate decoupling performance.

Fig. 13(c) and (d) show the estimated rotor position of the two winding sets and the corresponding position error value with the actual position, respectively. It can be seen that the proposed EDC architecture method can accurately estimate the rotor position value in the dynamic process of current sharing, and the position error is restricted within 5°.

For comparative analysis, Fig. 14(a) and (b) show the experimental results of the conventional sensorless control algorithm under the failure of the interconnected communication cables

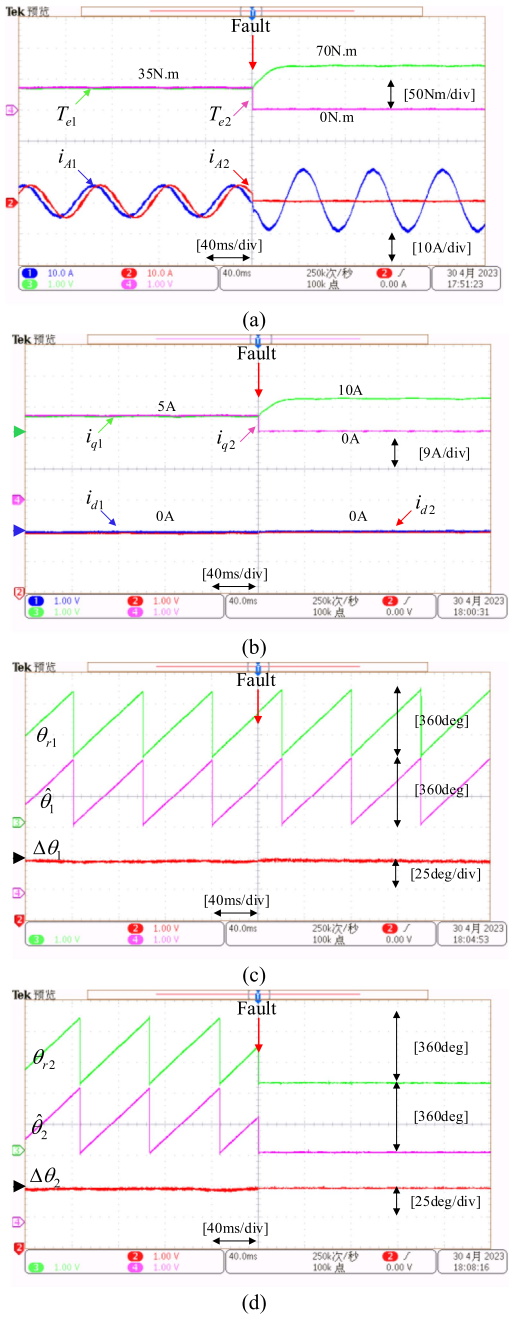

Fig. 15. Experimental results of a sudden inverter fault on the DTP-PMSG based on the proposed EDC architecture method. (a) Phase current and torque waveform. (b) dq -axis currents. (c) Actual rotor position θ_{r1}, estimated rotor position $\hat{\theta}_1$, and corresponding position error $\Delta\theta_1$ of the first set of windings. (d) Actual rotor position θ_{r2}, estimated rotor position $\hat{\theta}_2$, and corresponding position error $\Delta\theta_2$ of the second set of windings.

in the conventional distributed control architecture. The given reference values are the same as that in Table II. As can be seen, when the conventional sensorless control is applied to the power unbalance condition, the position error between the estimated rotor position and the actual value even exceeds 30°, which makes it impossible to use the estimated rotor position for closed-loop control. From the comparison between Figs. 13 and 14, it can be proved that the proposed EDSC method in EDC architecture can be well applied to power and current unbalance conditions.

The experimental results, which are consistent with the simulation results, support the conclusion that the proposed EDC architecture can achieve effective dynamic and steady-state control without the interconnected communication cables.

F. Experimental Results of a Sudden Inverter Fault

To verify the operational performance of the proposed EDC architecture method in the event of inverter failure, Fig. 15 shows the experimental waveforms of the DTP-PMSG when experiencing inverter faults during normal operation. To simulate a fault condition, a hardware fault signal is artificially sent to Inverter 2, which triggers its hardware protection circuit and causes it to stop operating. Prior to the fault occurrence, the given reference q-axis currents of the two winding sets are $i_{q1}^* = i_{q2}^* = 5$ A, and the given currents for the d-axis are set to 0 A. After the fault occurs, the health status S_2 in (7) will change from 1 to 0, and the given reference q-axis current of the first winding set is adjusted to $i_{q1}^* = 10$ A to maintain the output power of the motor unchanged.

It can be seen from Fig. 15(a) and (b) that the proposed EDC architecture can timely disconnect the faulty inverter while preserving the normal operation of the healthy inverter and winding set. Furthermore, it can quickly track the given current command, ensuring that the total output power of the DTP-PMSG remains unchanged after the occurrence of inverter failure. The rotor information in Fig. 15(c) and (d) show that the proposed EDSC method can accurately estimate the rotor position under inverter fault conditions, with the rotor position error being within 5°. From the experimental results in Fig. 15, it is evident that the proposed EDC architecture method can effectively handle the working conditions of inverter faults and exhibits good fault-tolerant control performance.

VI. Conclusion

To solve the problem caused by the communication failure of interconnected communication cables under the conventional distributed control architecture, this article proposes an EDC architecture of the MTP-PMSG that eliminates the need for interconnected communication cables and improves redundancy. The fundamental principle of this proposed method is to transform the coupling characteristics between the MTP-PMSG winding sets under different current distributions into variations in the inductance parameters of the winding set. Compared with the conventional distributed control architecture, the proposed EDC architecture method can achieve decoupling between the MTP-PMSG winding sets without interconnecting communication cables, and accurately estimate the rotor position of each winding set of the MTP-PMSG under power-sharing conditions. The contributions of this article are as follows.

1) The decoupling mathematical model of the MTP-PMSG in the EDC architecture is derived by introducing the current ratio parameter, which transforms the coupling between winding sets into the change of equivalent inductance parameters.

2) A novel EDSC method is proposed based on the EDC architecture, which can accurately estimate the rotor position under the condition of power balance or unbalance between winding sets.
3) The harmonic mathematical model of the DTP-PMSG is analyzed, which proves that the harmonic model also has electromagnetic coupling between winding sets. And then a MFPHC suppression method is given to realize the stator current harmonic suppression under the EDC architecture.

The research in this article can not only fully utilize the advantages of the high redundancy of the MTP-PMSG topology, but also serve as a supplement to conventional distributed control in the event of interconnected communication cables failure. One limitation is that it may reduce the degree of controllability from a control perspective. The comparative simulation and experimental results demonstrate that the proposed EDC architecture method can achieve effective and stable operation in both stable and dynamic conditions with arbitrary current sharing of winding sets.

REFERENCES

[1] G. Ning et al., "A hybrid resonant ZVZCS three-level converter for MVDC-connected offshore wind power collection systems," *IEEE Trans. Power Electron.*, vol. 33, no. 8, pp. 6633–6645, Aug. 2018.

[2] I. Jlassi and A. J. Cardoso, "Enhanced and computationally efficient model predictive flux and power control of PMSG drives for wind turbine applications," *IEEE Trans. Ind. Electron.*, vol. 68, no. 8, pp. 6574–6583, Aug. 2021.

[3] M. A. Parker, L. Ran, and S. J. Finney, "Distributed control of a fault-tolerant modular multilevel inverter for direct-drive wind turbine grid interfacing," *IEEE Trans. Ind. Electron.*, vol. 60, no. 2, pp. 509–522, Feb. 2013.

[4] Z. Wang, Y. Wang, J. Chen, and M. Cheng, "Fault-tolerant control of NPC three-level inverters-fed double-stator-winding PMSM drives based on vector space decomposition," *IEEE Trans. Ind. Electron.*, vol. 64, no. 11, pp. 8446–8458, Nov. 2017.

[5] Y. Gang, G. Yichang, Z. Lidan, L. Dongdong, and L. Xing, "Multi-phase permanent magnet synchronous generator variable speed constant frequency offshore wind system based on modular multilevel converter," in *Proc. IEEE Innov. Smart Grid Technol. Asia*, 2019, pp. 2127–2132.

[6] F. Luise, S. Pieri, M. Mezzarobba, and A. Tessarolo, "Regenerative testing of a concentrated-winding permanent-magnet synchronous machine for offshore wind generation—Part I: Test concept and analysis," *IEEE Trans. Ind. Appl.*, vol. 48, no. 6, pp. 1779–1790, Nov./Dec. 2012.

[7] M. J. Duran, I. González-Prieto, A. González-Prieto, and F. Barrero, "Multiphase energy conversion systems connected to microgrids with unequal power-sharing capability," *IEEE Trans. Energy Convers.*, vol. 32, no. 4, pp. 1386–1395, Dec. 2017.

[8] A. S. Abdel-Khalik, A. M. Massoud, and S. Ahmed, "Nine-phase six-terminal induction machine modeling using vector space decomposition," *IEEE Trans. Ind. Electron.*, vol. 66, no. 2, pp. 988–1000, Feb. 2019.

[9] A. S. Abdel-Khalik, A. M. Massoud, and S. Ahmed, "An improved torque density pseudo six-phase induction machine using a quadruple three-phase stator winding," *IEEE Trans. Ind. Electron.*, vol. 67, no. 3, pp. 1855–1866, Mar. 2020.

[10] I. Zoric, M. Jones, and E. Levi, "Arbitrary power sharing among three-phase winding sets of multiphase machines," *IEEE Trans. Ind. Electron.*, vol. 65, no. 2, pp. 1128–1139, Feb. 2018.

[11] L. De Camillis, M. Matuonto, A. Monti, and A. Vignati, "Optimizing current control performance in double winding asynchronous motors in large power inverter drives," *IEEE Trans. Power Electron.*, vol. 16, no. 5, pp. 676–685, Sep. 2001.

[12] W. Liao, M. Lyu, S. Huang, Y. Wen, M. Li, and S. Huang, "An enhanced SVPWM strategy based on vector space decomposition for dual three-phase machines fed by two DC-source VSIs," *IEEE Trans. Power Electron.*, vol. 36, no. 8, pp. 9312–9321, Aug. 2021.

[13] K. Alewine and W. Chen, "A review of electrical winding failures in wind turbine generators," *IEEE Elect. Insul. Mag.*, vol. 28, no. 4, pp. 8–13, Jul./Aug. 2012.

[14] I. Subotic, O. Dordevic, J. B. Gomm, and E. Levi, "Active and reactive power sharing between three-phase winding sets of a multiphase induction machine," *IEEE Trans. Energy Convers.*, vol. 34, no. 3, pp. 1401–1410, Sep. 2019.

[15] C. Zhang, W. Ma, and C. Sun, "A switchable high-speed fiber-optic ring net topology and its method of high-performance synchronization for large-capacity power electronics system," *Int. J. Elect. Power Energy Syst.*, vol. 57, pp. 335–349, 2014.

[16] Y. Nan et al., "Real-time monitoring of wind-induced vibration of high-voltage transmission tower using an optical fiber sensing system," *IEEE Trans. Instrum. Meas.*, vol. 69, no. 1, pp. 268–274, Jan. 2020.

[17] S. Umans, *Fitzgerald & Kingsley's Electric Machinery*. New York, NY, USA: McGraw-Hill, 2013.

[18] J. H. Teng, S. H. Liao, W. H. Huang, and C.-C. Chiang, "Smart control strategy for conversion efficiency enhancement of parallel inverters at light loads," *IEEE Trans. Ind. Electron.*, vol. 63, no. 12, pp. 7586–7596, Dec. 2016.

[19] Y. Hu, Z. Q. Zhu, and M. Odavic, "Comparison of two-individual current control and vector space decomposition control for dual three-phase PMSM," *IEEE Trans. Ind. Appl.*, vol. 53, no. 5, pp. 4483–4492, Sep./Oct. 2017.

[20] G. Liang et al., "An optimized pulsewidth modulation for dual three-phase PMSM under low carrier ratio," *IEEE Trans. Power Electron.*, vol. 37, no. 3, pp. 3062–3072, Mar. 2022.

[21] J. Han, "From PID to active disturbance rejection control," *IEEE Trans. Ind. Electron.*, vol. 56, no. 3, pp. 900–906, Mar. 2009.

[22] S. Chen, W. Ding, R. Hu, X. Wu, and S. Shi, "Sensorless control of PMSM drives using reduced order quasi resonant-based ESO and Newton–Raphson method-based PLL," *IEEE Trans. Power Electron.*, vol. 38, no. 1, pp. 229–244, Jan. 2023.

[23] Y. Zhang, T. Jiang, and J. Jiao, "Model-free predictive current control of DFIG based on an extended state observer under unbalanced and distorted grid," *IEEE Trans. Power Electron.*, vol. 35, no. 8, pp. 8130–8139, Aug. 2020.

[24] M. Fliess and C. Join, "Model-free control," *Int. J. Control*, vol. 86, no. 12, pp. 2228–2252, 2013.

[25] J. Karttunen, S. Kallio, P. Peltoniemi, P. Silventoinen, and O. Pyrhönen, "Decoupled vector control scheme for dual three-phase permanent magnet synchronous machines," *IEEE Trans. Power Electron.*, vol. 61, no. 5, pp. 2185–2196, May 2014.

[26] T. Liu, Z. Q. Zhu, Z.-Y. Wu, D. Stone, and M. Foster, "A simple sensorless position error correction method for dual three-phase permanent magnet synchronous machines," *IEEE Trans. Energy Convers.*, vol. 36, no. 2, pp. 895–906, Jun. 2021.

[27] L. Yan et al., "Multiple synchronous reference frame current harmonic regulation of dual three phase PMSM with enhanced dynamic performance and system stability," *IEEE Trans. Ind. Electron.*, vol. 69, no. 9, pp. 8825–8838, Sep. 2022.

[28] T. M. Jahns, G. B. Kliman, and T. W. Neumann, "Interior permanent magnet synchronous motors for adjustable-speed drives," *IEEE Trans. Ind. Appl.*, vol. IA-22, no. 4, pp. 738–747, Jul. 1986.

[29] T. Liu, Z. Q. Zhu, X. Wu, Z. Wu, D. A. Stone, and M. P. Foste, "A position error correction method for sensorless control of dual three-phase permanent magnet synchronous machines," *IEEE Trans. Ind. Appl.*, vol. 58, no. 3, pp. 3589–3601, May/Jun. 2022.

[30] G. Feng, C. Lai, W. Li, Z. Li, and N. C. Kar, "Dual reference frame based current harmonic minimization for dual three-phase PMSM considering inverter voltage limit," *IEEE Trans. Power Electron.*, vol. 36, no. 7, pp. 8055–8066, Jul. 2021.

[31] B. Zheng, J. Zou, B. Li, M. Tang, Y. Xu, and P. Zanchetta, "Analysis and fault-tolerant control for dual-three-phase PMSM based on virtual healthy model," *IEEE Trans. Power Electron.*, vol. 37, no. 12, pp. 15411–15424, Dec. 2022.

[32] Y. Zhao and T. A. Lipo, "Space vector PWM control of dual three-phase induction machine using vector space decomposition," *IEEE Trans. Ind. Appl.*, vol. 31, no. 5, pp. 1100–1109, Sep./Oct. 1995.

[33] Y. Hu, Z. Q. Zhu, and K. Liu, "Current control for dual three-phase permanent magnet synchronous motors accounting for current unbalance and harmonics," *IEEE J. Emerg. Sel. Topics Power Electron.*, vol. 2, no. 2, pp. 272–284, Jun. 2014.

[34] A. Galassini, A. Costabeber, M. Degano, C. Gerada, A. Tessarolo, and R. Menis, "Enhanced power sharing transient with droop controllers for multithree-phase synchronous electrical machines," *IEEE Trans. Ind. Electron.*, vol. 66, no. 7, pp. 5600–5610, Jul. 2019.
[35] S. Rubino, R. Bojoi, D. Cittanti, and L. Zarri, "Decoupled and modular torque control of multi-three-phase induction motor drives," *IEEE Trans. Ind. Appl.*, vol. 56, no. 4, pp. 3831–3845, Jul./Aug. 2020.
[36] X. Peng, Z. Liu, and D. Jiang, "A review of multiphase energy conversion in wind power generation," *Renewable Sustain. Energy Rev.*, vol. 147, no. 2, Sep. 2021, Art. no. 111172.
[37] Z. Ji, S. Cheng, Q. Ren, X. Li, Y. Lv, and D. Wang, "The effects and mechanisms of periodic-carrier-frequency PWM on vibrations of multiphase permanent magnet synchronous motors," *IEEE Trans. Power Electron.*, vol. 38, no. 7, pp. 8696–8706, Jul. 2023, doi: 10.1109/TPEL.2023.3260647.
[38] G. Liu, B. Chen, K. Wang, and X. Song, "Selective current harmonic suppression for high-speed PMSM based on high-precision harmonic detection method," *IEEE Trans. Ind. Inform.*, vol. 15, no. 6, pp. 3457–3468, Jun. 2019.

Ge Liang was born in Qinzhou, China, in 1996. He received the B.S. degree in electrical engineering in 2018 from the College of Electrical and Information Engineering, Hunan University, Changsha, China, where he is currently working toward the Ph.D. degree in electrical engineering.

His current research interests include advanced control of permanent magnet synchronous motor drive.

Sheng Huang received the M.S. and Ph.D. degrees in electrical engineering from the College of Electrical and Information Engineering, Hunan University, Changsha, China, in 2012 and 2016, respectively.

He is currently a Professor with the College of Electrical and Information Engineering, Hunan University. His research interests include renewable energy generation, modeling and integration study of wind power, control of energy storage system, and voltage control.

Wu Liao received the B.S. degree in automation and the Ph.D. degree in electrical engineering from Hunan University, Changsha, China, in 2010 and 2016, respectively.

From 2016 to 2019, he was with CRRC Zhuzhou Institute Company, Ltd., Zhuzhou, China, as a Converter Software Designer and Researcher. From 2019 to 2022, he was a Postdoc with the College of Electrical and Information Engineering, Hunan University, where he is currently an Associate Professor. His research interests include wind power system, high power motor drives.

Yu Liu (Graduate Student Member, IEEE) received the B.S. degree in electrical engineering from Hunan Institute of Engineering, Xiangtan, China, in 2017 and the M.S. degree in electrical engineering in 2020 from the College of Electrical and Information Engineering, Hunan University, Changsha, China, where he is currently working toward the Ph.D. degree in electrical engineering.

His current research interests include advanced control of permanent magnet synchronous motor drive.

Congqi Feng (Graduate Student Member, IEEE) received the B.S. degree in electrical engineering from China University of Mining and Technology, Xuzhou, China, in 2020. He is currently working toward the Ph.D. degree in electrical engineering with the College of Electrical and Information Engineering, Hunan University, Changsha, China.

His current research interests include advanced control of permanent magnet synchronous motor drive.

Xuan Wu was born in Hunan, China, in 1983. He received the M.S. and Ph.D. degrees in automation from the College of Electrical and Information Engineering, Hunan University, Changsha, China, in 2011 and 2016, respectively.

From 2016 to 2019, he was a Postdoc with the College of Electrical and Information Engineering, Hunan University, where he is currently an Associate Professor. His research interests include permanent magnet synchronous motor drives and position sensorless control of ac motors.

Shoudao Huang (Senior Member, IEEE) received the B.E. and Ph.D. degrees in electrical engineering from Hunan University, Changsha, China, in 1982 and 2003, respectively.

He is currently a Professor with the College of Electrical and Information Engineering, Hunan University. His research interests include motor drives, power electronics, and control systems.